FOV effect analysis in directional brightness temperature observations for urban targets

ZHAN Wenfeng[1], CHEN Yunhao[1], MA Wei[1, 2], ZHOU Ji[1], LI Jing[1]

1. *State Key Laboratory of Earth Surface Processes and Resource Ecology*, *College Institute of Resources Science & Technology*, *Beijing Normal University*, *Beijing* 100875, *China*;
2. *Institute of Mineral Resources Research*, *China Metallurgical Geology Bureau*, *Beijing* 100029, *China*

Abstract: Thermal anisotropy regime for urban targets was investigated using a simplified urban structure model based on the radiosity principles and OpenGL. Each component fraction's variation regime was examined by computer simulation in different observation zeniths, azimuths and distances between the sensor and targets. Results indicate that: (1) significant field of view (FOV) effect exists in the DBT (directional brightness temperature) ground-based platform observations. It is able to reach the maximum values near the plane perpendicular to the solar main plane. (2) Analysis about FOV effect for a physical model of typical urban surface and cover patterns at different spatial locations and time series reveals that it can achieve several centigrade or so in a sunny day. (3) There is a significant "scale effect" in near-ground observations and it varies along with the distance between the sensor and urban targets. (4) The FOV effect cannot be neglected in comparisons between DBTs observed in ground-based field experiments and in images acquired from satellites.

Key words: thermal infrared remote sensing, field of view effects, directional brightness temperature, radiosity model

CLC number: TP79 **Document code:** A

Citation format: Zhan W F, Chen Y H, Ma W, Zhou J and Li J. 2010. FOV effect analysis in directional brightness temperature observations for urban targets. *Journal of Remote Sensing*. **14**(2): 372—386

1 INTRODUCTION

Urban surface temperature is a key parameter for urban climates. Understanding thermal anisotropy regime for urban surfaces is necessary for accurate estimation of surface temperature distribution since different DBTs (Directional Brightness Temperature) of the same targets are observed from remote sensing multi-angular thermal sensors. Thermal anisotropy of urban targets is closed related with the sun-urban surface targets-sensors geometrical conditions, urban structure and physical properties of ground targets (Zhou *et al.*, 2009). In addition, it is strongly influenced by the scope of FOV (field of view), components emissivities anisotropy and environmental irradiance (Lagouarde *et al.*, 1995; Wang *et al.*, 2000; Voogt & Oke, 2003; Fan *et al.*, 2003). This effect, which suggests different parts of the same target are "seen" and different DBTs are measured due to FOV variation, is named as FOV effect (Zhang *et al.*, 2000; Yu *et al.*, 2004; Huang *et al.*, 2007a, 2007b).

In order to eliminate the influence of FOV effect, Zhang *et al.* (2000) proposed a so-called "thermal imager-fix area method". The distance between the thermal sensor and observation targets is always limited in near-ground DBT measurements for urban surfaces, sensors with broad FOVs were usually used since land cover patterns in FOVs were then representative in such an extreme condition (Soux *et al.*, 2003; Lagouarde *et al.*, 2004; Voogt, 2008). However, there are great differences in imaging mode between near-ground platforms and satellite levels. The FOV for a single pixel observed from the satellite level is extremely narrow and the distance between the sensor and the targets is enormous compared with the size of the pixel, all of which will lead to the change of observation targets and result in significant FOV effect. This phenomenon attracts many researchers' interests. Yu *et al.* (2004) preliminarily analyzed FOV effect of row crops using a simplified two-dimensional structure. Li L *et al.* (2006) studied row crop FOV effects based on a grid model. However, further studies are still necessary for FOV effect estimation.

Currently, quantitative researches about FOV effect mainly concentrated on vegetations. Researches for urban targets are still relatively rare. In addition, many studies are still limited to two-dimensional simulations. In this study, the component fractions of urban targets in FOV were simulated using a simplified three-dimensional urban structure model based on the OpenGL and radiosity principles (Soux *et al.*, 2003; Voogt,

Received: 2008-12-24; **Accepted**: 2009-03-05

Foundation: National Natural Science Foundation of China (No. 40771136, No. 40701114) and Excellent People Cultivation Foundation in Beijing (No. 20081D0503100254).

First author biography: ZHAN Wenfeng (1986—), male, Ph. D candidate. He received his bachelor's degree in Wuhan University, 2007. He majors in application of remote sensing in resource and environment. E-mail: zhanwenfeng@ires.cn

Corresponding author: CHEN Yunhao, E-mail: cyh@ires.cn

2008; Ma *et al.*, 2008). Combined with component temperatures and DBTs observed from field experiments and physical models for urban targets, the extent and impacts of FOV effects have been examined thoroughly based on simulations of DBTs observed by sensors onboard satellites and near-ground platforms.

2 METHODOLOGY

2.1 DBT and component temperature

The directional radiance acquired by a sensor can be modeled by the following equation (Noman & Becker, 1995):

$$B_{\mathrm{b},i}(\theta,\phi)=\int_{\lambda_1}^{\lambda_2}\frac{f_i(\lambda)C_1}{\pi\lambda^5[\exp(\frac{C_2}{\lambda T_{\mathrm{b},i}(\theta,\phi)})-1]}\mathrm{d}\lambda \quad (1)$$

where $B(T_{\mathrm{b},i}(\theta,\phi))$ is the directional radiance, λ_1 and λ_2 are the lower and upper wavelengths of the IRT (infrared thermometer) in channel i, respectively. $f_i(\lambda)$ is the spectral response of the IRT detector. C_1=3.7404×10^{8}W·μm^4·m^{-2}; C_2=14387μm·K; $T_{\mathrm{b},i}(\theta,\phi)$ is the brightness temperature in the corresponding channel.

Based on the assumption that a pixel is composed by several components, the relationship between DBT of the targets and component temperatures in such a pixel satisfies the following formula (Menenti *et al.*, 2008; Yu *et al.*, 2006a; Huang *et al.*, 2007b):

$$B_\lambda(T_{\mathrm{b}}(\theta,\phi))=\sum_{k=1}^{N}f_k(\theta,\phi)\varepsilon_k B_\lambda(T_k) \quad (2)$$

where $B_\lambda(T_{\mathrm{b}}(\theta,\phi))$ is the Plank's function; $T_{\mathrm{b}}(\theta,\phi)$ is the directional brightness temperature; $f_{\mathrm{k}}(\theta,\phi)$ is the fraction of a certain component k, and $f_1+f_2+\ldots+f_N=1$; ε_k is the emissivity of component k; T_k is the component temperature. Eq. (2) reveals that component classification criterion and the fraction of each component are two main factors that influencing the directional brightness temperature.

2.2 Simplification for urban targets

Typical urban targets were simplified into a series of three-dimensional rectangular elements in this study (Soux *et al.*, 2003; Ma *et al.*, 2009) and the radiosity was utilized to calculate different component-fraction areas. In Fig. 1, O is the sensor; S_1 represents the area in a single pixel of an image acquired from a satellite infrared sensor, which may consist of varieties of urban surfaces; S_2 is a hemisphere centralized at O and have a radius equals to 1 unit; while S_3 is the "equivalent focal plane" of the sensor. P_1 is the roof of a building, and P_2 represents the projection curved surface of the building roof in S_2; P_3 is the projection of P_2 in "equivalent focal plane" S_3.

The components fraction of the roof f_{roof} can be expressed analytically as follows (Baum *et al.*, 1989):

$$f_{\mathrm{roof}}=\frac{1}{2\pi}\sum_{i=0}^{3}|\boldsymbol{\Psi}\cdot\boldsymbol{\Gamma}_i| \quad (3)$$

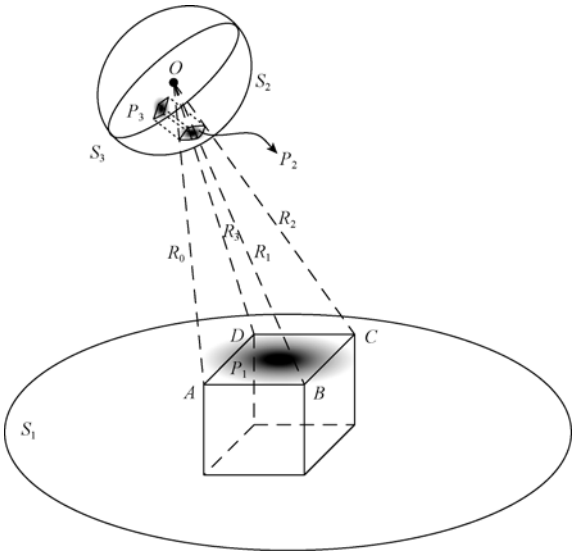

Fig. 1 Geometrical meaning of component fractions (Sun *et al.*, 2005)

where $\boldsymbol{\Psi}$ is the normalized vector of S_3, the magnitude of $\boldsymbol{\Gamma}_i$ equals to the angle $\boldsymbol{\delta}_i$ formed by the vectors $\boldsymbol{R}_i$ and $\boldsymbol{R}_{i+1}$, which is measured by radians; while the direction is given by the cross product of vectors $\boldsymbol{R}_i$ and $\boldsymbol{R}_{i+1}$. The geometrical significance of component fraction f_{roof} means the ratio between P_3 and S_3 (Sun *et al.*, 2005).

3 COMPONENT FRACTION SIMULATION

Research has shown that component physical properties, weather being illuminated by sun, the angle formed by sun light and component plane are main factors influencing the temperature features and variation of urban targets. (Jackson *et al.*, 1979; Li & Strahler, 1985; Li *et al.*, 1995; Yu *et al.*, 2005). Yu *et al.* (2006b) divided the urban surface into five classes: light-soil, dark-soil, light-roof, dark-roof, light-wall and dark-wall according to his field observation. Based on the similar regulations, the typical urban targets were partitioned into five classes in our study: light-ground, dark-ground, light-roof, light-wall and dark-wall on the basis of our field experiments using the infrared thermometer (Ma *et al.*, 2008).

After some detailed survey and statistics for buildings' sizes, directions and the street widths, some typical urban residential blocks in Beijing metropolitan area were selected for analyzing urban thermal anisotropy, we used a computational model to simulate the fractions of varieties of components based on the "Urban Targets Entity model" produced in 3DSMax (Ma *et al.*, 2008). The main modeling parameters are listed as follows in Table 1.

3.1 Viewpoint located on satellite level

When the viewpoint is located on satellite levels, FOV (field of view) for a single pixel in an image is extremely narrow, and the distance between the senor and targets is almost infinite versus near-ground platforms. Fig. 2 shows a fraction-

Table 1 Attribute parameters of simulation model

Model parameters	Value
Observation time	2008-08-22 10:40 am (local time, beijing)
Building width from east to west /m	15
Street width from east to west /m	5
Building width from north to south /m	10
Street width from north to south /m	12.5
Building height /m	13
FOV /(°)	20

polarization graphs of sunlit walls and shadow walls when the senor is on the satellite. The angular-coordinate is the sensor azimuth ranging from 0° to 360°, while the distance-coordinate is the sensor zenith that ranges from 0 ° to 60 °. *S* is the location of the sun.

Fig. 2 demonstrates that the extreme values of light-wall and dark-wall in the polarization graph almost lied near the solar main plane, which indicates that these two components fractions are strongly influence by sun position. For sunlit walls, the maximum values concentrate near the "hotspot", whereas the shadow walls have opposite features. On the other hand, these two components have a definite "step" feature along with the azimuth angle, while they have not such clear characteristics in zenith angle. For instance, the sun position at 10:40 am is shown in Fig. 2(a), the component fraction of sunlit walls is low when azimuth ranges from 270° to 360°, but its value increases rapidly when the azimuth φ equals 270° or 360°. Similarly, the sun position at 14:30 pm is illustrated in Fig. 2(b); component fraction of sunlit walls is low when azimuth ranges from 90° to 180°, but its values change abruptly at the edge when the azimuth φ equals 90° or 180°.

Since azimuth of the sun ranged from 90° to 270° between these two moments, average values of sunlit grounds are higher in south hemi-plane than in north hemi-plane, while the shadow grounds is contrast to sunlit grounds. These two components were not influenced apparently by sun position compared with sunlit and shadow walls.

3.2 Viewpoint located near-ground

3.2.1 Variation of zenith and azimuth

Compared with the viewpoint being located on satellite levels, the limited distance between the sensor and targets will lead to abrupt variation of component fraction in DBT observations when the thermal imager is from near ground platforms. Fig. 3 shows the component fraction-polar plot when the senor is located near the ground (IFOV = 17°; observation distance = 300m). The range of azimuth and zenith is the same as Fig. 2. *S* represents the sun position n in Fig. 3.

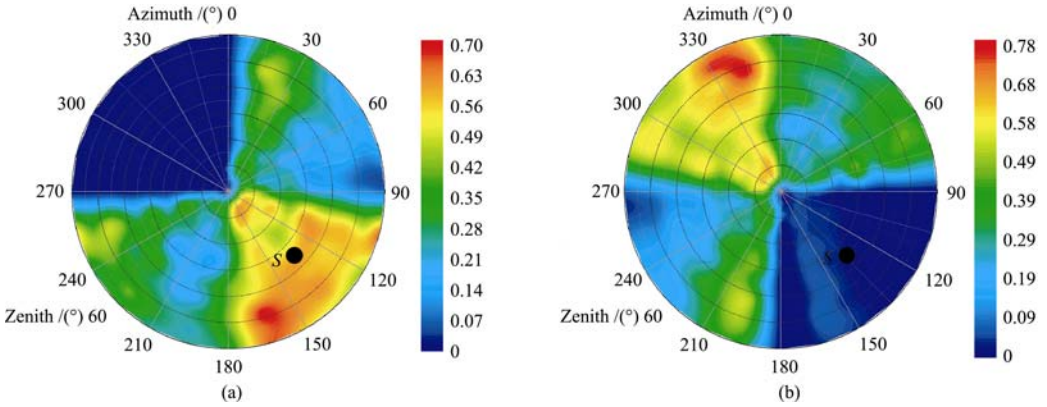

Fig. 2 Component fraction-polarization figure when the senor is on the satellite level

(a) Sunlit walls; (b) Shadow walls

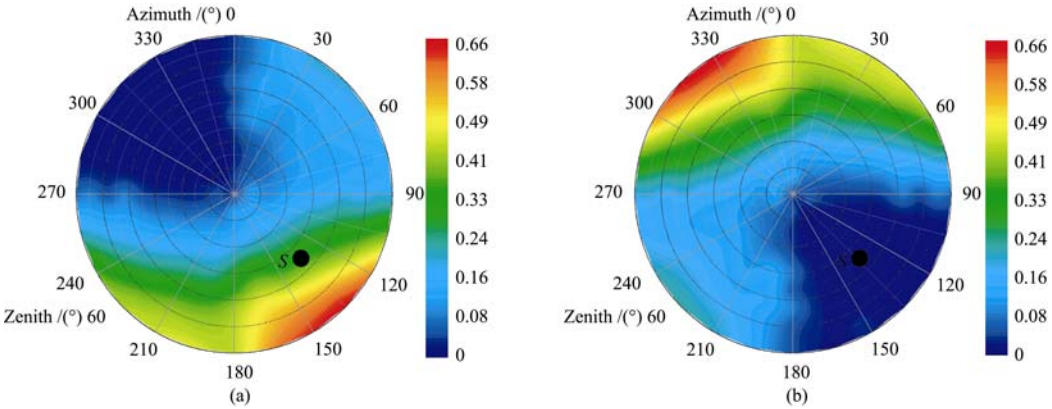

Fig. 3 Component fraction-polar plots of the sensors from near-ground platforms (IFOV = 17°; observation distance = 300m)

(a) Sunlit walls; (b) Shadow walls

From Fig. 3, sunlit walls and shadow walls are still strongly influenced by sun's position. The distribution component fractions for sunlit and shadow walls are similar to Fig. 2, but the minimum values in Fig. 3 distributed in a more extensive region and its "step" feature is not as distinctive as in Fig. 2. Furthermore, the component fraction changes more slowly relative to Fig. 2.

More simulation and analysis has manifested that the component fraction of sunlit roof is not influenced by sun position, its variation ranges from 0.30—0.38, narrower than in the condition when thermal imager is located on satellite level. Differential values between near-ground and satellites are high enough and they do not have the same distribution rule in polarization figure. This phenomenon also suggests apparent FOV effect exists in field DBT observation experiments.

3.2.2 Variation of observation distance

Fig. 4 demonstrates the change of component fraction along with the observation distance (the observation zenith and azimuth are 10° and 120° respectively), where the distance between thermal imager and the targets represents x-coordinate (unit: m); while component fraction value is the y-coordinate. The solid line in Fig. 4 denotes the component fraction when viewpoint is situated on a satellite.

Fig. 4 shows that component fraction take a rapid change along with the increase of distance between thermal imager and the targets. It is reasonable that the sunlit wall component fraction is higher than the shadow wall because the viewpoint situates in the direction of sun (hotspot direction). Since the shadow walls component fraction is so low that it alternates slightly with distance's increase. The differential values between near-ground and on satellite level are negligible when the observation distance is 800m if the modeling parameters are designed as in Table 1, this will be proved again in the following experiments and validation.

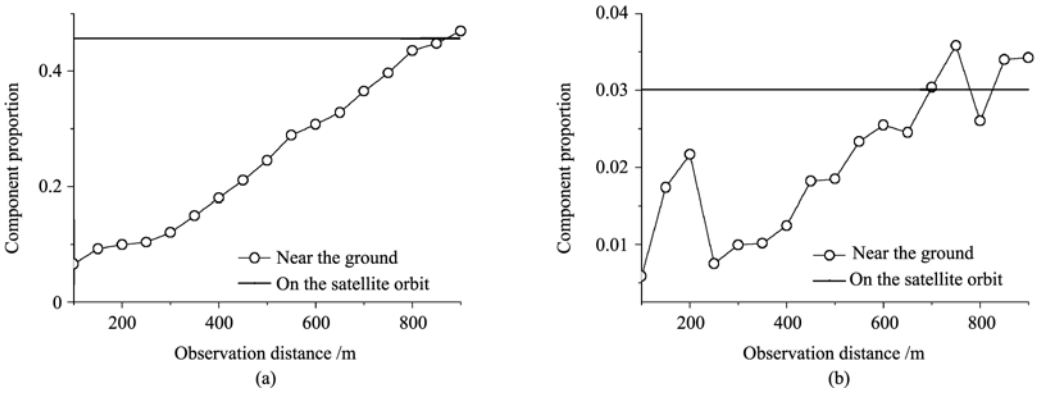

Fig. 4 Variation of components fractions along with the observation distance (the observation zenith and azimuth are 10° and 120° respectively)
(a) Sunlit walls; (b) Shadow walls

4 EXPERIMENTS AND VALIDATION

A new concept named DBTDV (Directional Brightness Temperature Differential Value) is defined for estimating the extent of FOV effect, implying the DBT differential values when thermal imager are located between near-ground and on satellites. FOV effect will be more evidently if the absolute DBTDV is higher, on the other hand, FOV effect will be less apparently in the opposite situation. Computational simulation about the component fractions is the basis of analyzing the extent of FOV effect, and it is necessary to calculate the DBTDV numerically and explore the FOV effect variation regime analytically in detail to measure this effect due to component fraction discrepancies between near-ground and on satellite levels.

Consequently, field observations were held at Fangshan experimental bases, Beijing Normal University in August, 2008. Multi-angle thermal infrared radiation near-ground observing system was designed and used in this experiment (shown in Fig. 5). The thermal imager holder could rotate angularly in accordance with the gauge for warranting accuracy. Blackbody was used to calibrate the thermal imager

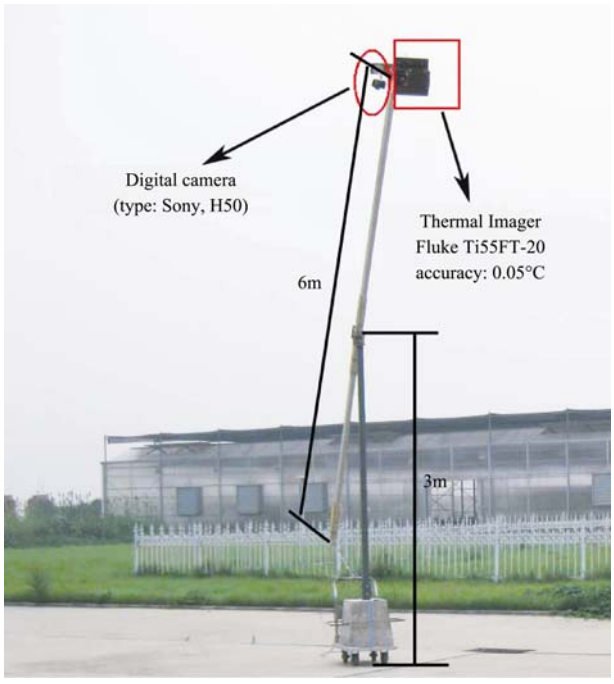

Fig. 5 Multi-angle thermal infrared radiation near-ground observing system

hanged at the end of the control-rod. Temperature values after calibrations were taken as the standard observation data. The thermal Imager is accurate enough (accuracy: 0.05℃) to satisfy the analysis and application.

The physical model is composed by some concrete cuboids about real urban targets with the scale 1∶50 and it was lined on the flat ground regularly (as shown in Fig. 6(a) and Fig. 6(b)). A round aluminum frame was utilized to denote the study area due to aluminum's low emissivity. The model-size parameters are shown in Table 1 (scale: 1∶50). Fig. 6(a) and Fig. 6(b) illustrate images of physical model about real urban targets in visible and thermal infrared band respectively. In Fig. 6(b), the brighter color represents the higher temperatures.

Field experiments and computational simulation are both used to analyze the FOV effect variation regime along with the zenith, azimuth and observation distance. Component temperatures are indispensable for input parameters in computational simulation model, so a portable infrared thermometer (type: Testo-845) was applied to measure component temperatures at 10:40 am and 14:30 pm respectively. The component temperatures are listed in the following Table 2 after a similar calibration for the IRT.

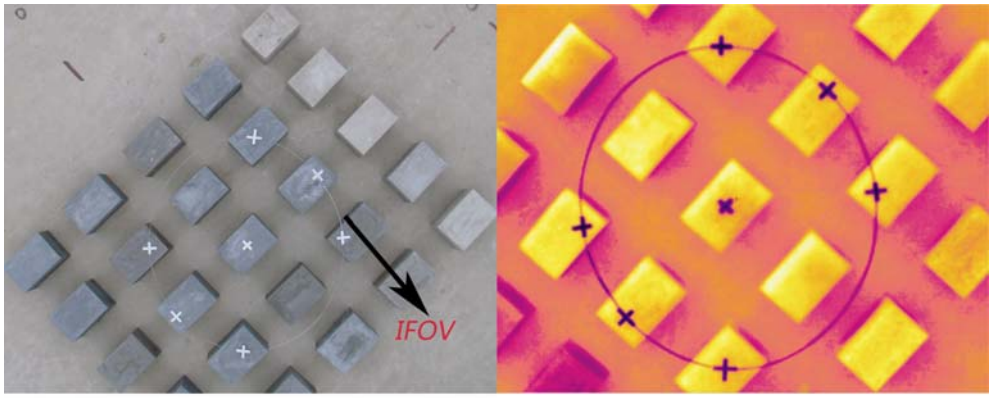

Fig. 6 Images of physical model about real urban targets in visible and thermal infrared band (the scope of IFOV is shown by an aluminum frame; scale: 1:50)
(a) Image in visible band; (b) Image in thermal band

Table 2 Temperatures of each component

Observation time	Sunlit ground /℃	Sunlit wall /℃	Sunlit roof /℃	Shadow ground /℃	Shadow wall /℃
10: 40	36.8	48.9	51.2	26.5	33.3
14: 30	41.0	48.2	50.3	30.7	37.0

4.1 FOV effect in different azimuths and zeniths

Fig. 7 shows the DBTDV-polar figures under the simulation model with component temperatures at 10:40 am and 14:30 pm respectively (the observation distance is 300m). The DBTDV at 10:40 am ranges from –4.42℃ to +3.18℃, most of the values lie between –1℃ to +1℃. While The DBTDV at 14:30 am varies from –3.18℃ to +3.46℃, which implies FOV effect in the morning is almost equivalent to that in the afternoon. *S* denotes the sun position; *P* represents the plane perpendicular to solar main plane. In Fig. 7(a) and Fig. 7(b), M_1 denotes the region holding the maximum values, by contrast, M_2 and M_3 represent the region provided with the minimum values. The extreme values of DBTDV lies near plane *P*, which indicates

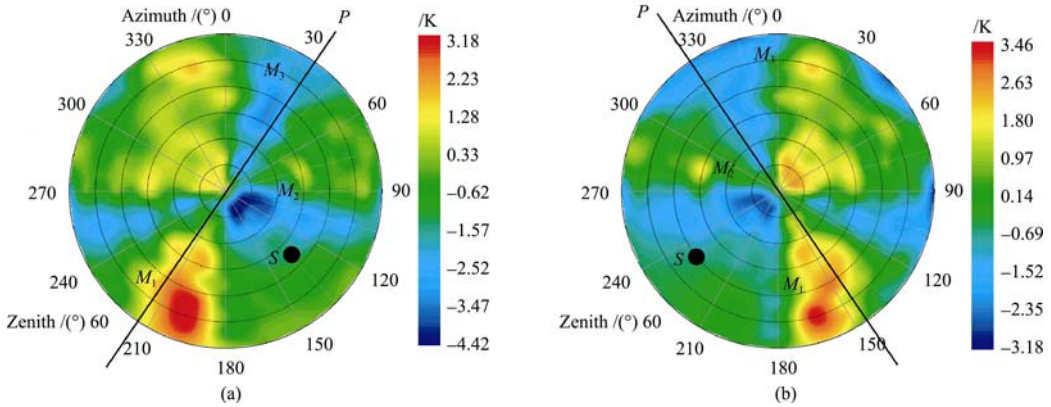

Fig. 7 DBTDV-polarization figure (the observation distance is 300m)
(a) 10:40 am; (b) 14:30 pm

FOV effect reaches the highest values near plane P when the IRT zenith angle θ<60°.

Wide FOVs are necessary when the sensor is from near-ground platforms, while it is extremely narrow corresponding to a single pixel when the sensor is on satellite levels. As been narrated before, this great discrepancies result in an apparent "Step" feature of component fraction distribution in Fig. 2 when $\varphi\in$ [0°, 90°] and $\varphi\in$ [180°, 270°]. By contrast with Fig. 2, component fraction varies slowly in those two intervals in Fig. 3. Consequently, this variance leads to a maximum FOV effect in the two intervals. The azimuth angle of the sun lies in [90°, 180°] in the morning, the solar main plane subjects to aggregate $\varphi\in${[90°, 180°],[270°, 360°]}, so the plane perpendicular to solar main plane belongs to the aggregate $\varphi\in${[0°, 90°],[180°, 270°]} (shown in Fig. 7(a)). It has an analogous relationship in the afternoon. In a word, FOV effect increases to the highest values near the plane P.

4.2 FOV effect in different distances

Combined with computational simulation results (computational simulation is the only way to obtain the field measurement DBT on the satellite orbit due to some well-known reasons), We made use of the Multi-angle thermal infrared radiation near-ground observing system for estimating the variance regime of DBTDV along with the observation distance. The results are demonstrated in Fig. 8 (a) and Fig. 8 (b), where the x-coordinate is the observation distance; DBTDV represents y-coordinate. In the morning simulation, solid azimuths and zeniths were selected in the areas M_1 (azimuth = 200°; zenith = 45°) and M_2 (azimuth = 120°; zenith = 10°) which had the extreme values; similarly, solid azimuths and zeniths were selected in the areas M_1 (azimuth = 150°; zenith = 40°) and M_2 (azimuth = 240°; zenith = 10°) at 14:30 pm.

Generally speaking, Fig. 8 (a) and Fig. 8 (b) have implied that FOV effect increases when the observation distance is lower; by contrast, FOV effect decreases if the observation distance is higher. FOV effect has a remarkable scale effect: resulted from observation distance, it is lower than 0.2℃ and could be negligible when the observation distance is higher than 800m; FOV effect (also means absolute DBTDV) has an inverse linear relationship with the observation distance when the distance ranges from 200m to 800m; if the distance is below 200m, the regime is more complicated, including both increasing abruptly (azimuth = 120°; zenith = 10° in Fig. 8(a) and azimuth = 240°; zenith = 10° in Fig. 8(b)) and decreasing slowly (azimuth = 200°; zenith = 45° in Fig. 8(a) and azimuth = 150°; zenith = 40° in Fig. 8 (b)) This is because the number of ground object category in the scope of FOV reduces continuously as the observation distance decreases to some extent; moreover, even just only one category of target is left when the observation distance is low enough, at this time, the DBT only depends on a certain component temperature. Although FOV effect is apparently high when the observation distance is lower than 200m because of the random distribution of component categories, the distribution regime is not as clearly as in the other two situations.

4.3 Time-series FOV effect

Field experiments data obtained from at 10:40 am to 12:00 am in August 23, 2008, were selected to analyze the variance of FOV effect in time series. The solar azimuth varied from 136° to 171° in this time period. The azimuth is divided into eight directions: east, west, south, north, northeast, southeast, southwest and northwest. Field observation experiments consisting of three turns according to different zeniths, eight directional observations were essential in every turn. Each observation lasted about 3 min; so it took 25 min approximately to carry out each turn.

Fig. 9 shows variance of DBTDV along with different observation angles in time series, where the order of measurement points denotes x-coordinate; DBTDV represents the y-coordinate. Almost all of the scatter points distribute around 0℃, DBTDV ranges from –3℃ to 4℃ and it has a similar variation span in each turn. FOV effect in the third turn is lower than in the first and the second turn, this may be derived from the minimum differential temperatures among components in respect that observation time was close to noon in the third turn. As demonstrated from Fig. 7 to Fig. 9, the results indicate that DBTDV of typical physical models ranges from –4℃ to +4℃ in different observation spatial location and moments.

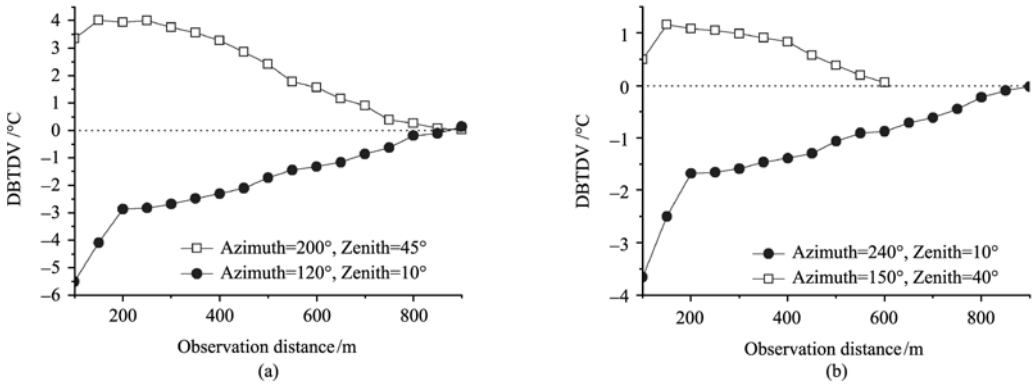

Fig. 8 Change of DBTDV along with the observation distance
(a) DBTDV at 10:40 am; (b) DBTDV at 14:30 pm

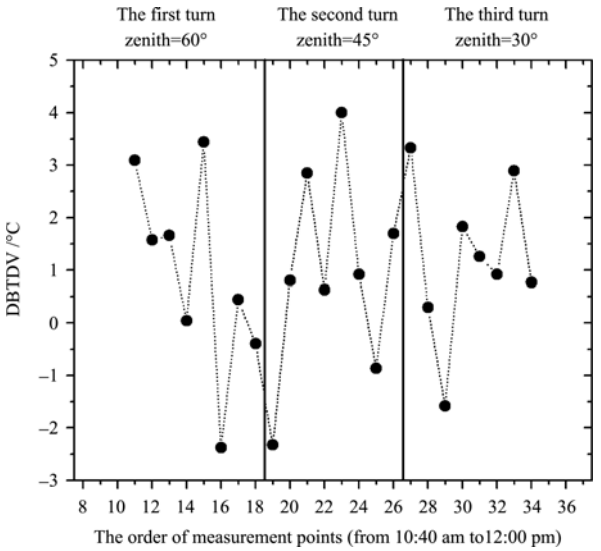

Fig. 9 Variance of DBTDV along with different observation angles in time series (obtained from 10:40 am to 12:00 pm; the observation distance is 300m)

5 CONCLUSION

The variations of the components fractions of typical urban targets in the FOV of the sensor onboard satellite level and near-ground platform corresponding with spatial locations were analyzed. The relationships between the FOV and view zenith, azimuth and distance between the sensor and target were investigated thoroughly. Results indicate that there was significant FOV effect when measuring the DBT of urban targets with near-ground platforms. FOV effect became most significant near the plane perpendicular to the solar main plane and it reduced rapidly when the distance increases. Furthermore, investigations about DBT in field measurements have made clear that FOV effect cannot be neglected for thermal anisotropy analysis.

The factors influencing FOV effect are so enormous that it is almost affected by all categories of ground objects: tall trees, low shrubs, grasslands, bare soil, roofs and walls with varieties of materials in typical urban surfaces, simple physical model is not appropriate anymore for representing all categories of land cover and land use patterns. Besides, surface-atmosphere is a coupled system, surface temperature distribution of each component is influenced profoundly by energy exchange between surface and atmosphere, and these bring out the complexity increasingly for inducing the variation regime of FOV effects. The scale effect is only examined qualitatively and primarily and there are still many deficiencies in quantitatively analyzing it for the FOV effect. The follow-up field validations and computer theoretical simulation studies are also being actively pursued.

REFERENCES

Baum D R, Rushmeier H E and Winget J M. 1989. Improving radiosity solutions through the use of analytically determined form-factors. *Computer Graphics*, **23**(3): 325—333

Fan W J and Xu X R. 2003. The Affecting factors of thermal radiant drectionality of the row winter wheat. *Geography and Geo-Information Science*, **19**(4): 84—88

Huang H G, Liu Q H, Liu Q, Du Y M and Li X W. 2007. Simulation of time effect on thermal emission directionality measurement. *Journal of System Simulation*, **19**(15): 3586—3590

Huang H G, Liu Q H, Liu Q, Xiao Q and Chen L F. 2007. Using multi-directional thermal images to obtain canopy component temperature and directional brightness temperature. *Journal of Beijing Normal University*(*Natural Science*), **643**(3): 292—297

Jackson R D, Raginato R J, Pinter P J, Jr and Sherwood B. I. 1979, Plant canopy information extracton from composite scene reflectance of row crops. *Applied Optics*, **18**(22): 3775—3782

Lagouarde J P, Kerr Y H and Brunet Y. 1995. An experimental study of angular effects on surface temperature for various plant canopies and bare soils. *Agricultural and Forest Meteorology*. **77**: 167—190

Lagouarde J P, Moreau P, Irvine M, Bonnefond J M, Voogt J A and Folliec F. 2004. Airborne experimental measurements of the angular variations in surface temperature over urban areas: case study of Marseille(France). *Remotes Sensing of Environment*, **93**: 443—462

Li L, Qiao Y L, Gu X F and Yu T. 2006. Field of view effect on the remote sensing field radiometric measurements. *Journal of Remote Sensing*, **10**(5): 676—682

Li X W and Strahler A. 1985. Geometric-optical modeling of a conifer forest canopy. *IEEE Trans Geosci Remote Sensing*, **23**(5): 705—721

Li X W and Wang J D. 1995. Optical Remote Sensing Model and Parameterization for Vegetation. Beijing: Science Press

Ma W, Chen Y H, Zhan W F and Zhou J. 2008. A computer model for simulating the thermal infrared radiation of 3-D urban targets. *Journal of Infrared and Millimeter Waves*, In Press

Menenti M, Li J and Li Z L. 2008. Multi-angular thermal infrared observations of terrestrial vegetation. Advances in Land Remote Sensing System, Modeling, Inversion and Application. Springer

Noman J M and Becker F. 1995. Terminology in thermal infrared remote sensing of natural surfaces. *Agricultural and Forest Meterology*, **77**: 153—166

Soux A, Voogt J A and Oke T R. 2003. A model to calculate what a remote sensor 'sees' of an urban surface. *Boundary-Layer Meteorology*, **111**: 109—132

Sun J G. 2005. Computer Graphics, Beijing: Tsinghua University Press

Voogt J A and Oke T R. 2003. Thermal remote sensing of urban climates. *Remote Sensing of Environment*. **86**: 370—384

Voogt J A. 2008. Assessment of an urban sensor view model for thermal anisotropy. *Remote Sensing of Environment*, **112**: 482—495

Wang J D, Li X W, Sun X M and Liu Q.2000. Component temperatures inversion for remote sensing pixel based on directional thermal radiation model. *Science in China(Ser. E),* **30**(supp.): 54—60

Yu T, Gu X F, Tian G L, Legrand M, Hanocq J F and Bosseno R. 2004. Analyzing the errors caused by FOV effect on the ground observations of drectional brightness temperature over a row Structured canopy. *Journal of Remote Sensing*, **8**(5): 443—450

Yu T, Gu X F, Tian G L, Legrand M, Hanocq J F, Bosseno R and Cai H Y. 2005. Study on the classification of component brightness temperature over a maize canopy. *Jounal of Remote Sensing*, **9**(1): 16—23

Yu T, Gu X F, Tian G L, Legrand M, Hanocq J F, Bosseno R, Cai H Y, Cheng T H and Yu S S. 2006. Modeling directional brightness temperature over a maize canopy in row structure. *Journal of Remote Sensing*, **10**(1): 15—20

Yu T, Tian Q Y, Gu X F, Wang J, Liu Q and Yan G J. 2006. Modelling directional brightness temperature over a simple typical structure of urban areas. *Journal of Remote Sensing*, **10**(5): 661—669

Zhang R H, Sun X M, Li Z L, Stoll M P, Su H B and Tang X Z. 2000. Revealing of major factors in the directional thermal radiation of ground objects. *Science in China*(*Ser. E*), **30**(supp.): 39—44

Zhou J, Chen Y H, Li J, Ma W and Zhan W F. 2009. Progress in thermal anisotropy of urban areas: a review. *Advances in Earth Science*, **24**(5):497—505

城市目标方向亮温观测的视场效应分析

占文凤[1], 陈云浩[1], 马 伟[1,2], 周 纪[1], 李 京[1]

1. 地表过程与资源生态国家重点实验室(北京师范大学), 北京师范大学 资源学院, 北京 100875;
2. 中国冶金地质总局 矿产资源研究院 遥感中心, 北京 100029

摘 要: 基于简化的城市目标三维结构模型, 利用计算机图形学中辐射度方法, 对城市目标的热辐射方向性规律进行模拟。在传感器分别位于近地面和卫星轨道时, 研究了城市目标各组分在视场内的权重随观测天顶角、方位角和观测距离改变的变化规律。结果表明: 城市目标方向亮温地面辐射测量存在显著视场效应。当传感器位于近地面时, 在垂直太阳主平面附近, 视场效应达到最大。方向亮温随观测距离的改变有明显变化。随着观测距离的增加, 视场效应急剧减小。将近地面测量得到的方向亮温与卫星影像计算所得的方向亮温对比时, 视场效应是一个必须考虑的因素。

关键词: 热红外遥感, 视场效应, 方向亮温, 辐射度模型

中图分类号: TP79 **文献标识码:** A

引用格式: 占文凤, 陈云浩, 马 伟, 周 纪, 李 京. 2010. 城市目标方向亮温观测的视场效应分析. 遥感学报, **14**(2): 372—386
Zhan W F, Chen Y H, Ma W, Zhou J and Li J. 2010. FOV effect analysis in directional brightness temperature observations for urban targets. *Journal of Remote Sensing*. **14**(2): 372—386

1 引 言

城市区域的热辐射方向性与太阳—地面目标—传感器的几何关系、城市形态与结构、地面目标物理性质等有密切关系(周纪等, 2008), 此外, 它还受到视场角范围、组分比辐射率的方向性和环境辐照度的影响(Lagouarde 等, 1995; 王锦地等, 2000; Voogt & Oke, 2003; 范闻捷等, 2003)。这种由视场变化导致地面观测目标发生变化, 从而影响方向亮温的效应称之为“视场效应”(张仁华等, 2000; 余涛等, 2004; 黄华国等, 2007a, 2007b)。

为了消除视场效应的影响, 张仁华等(2000)提出了热像仪——定面积法, 这种方法能一定程度地削弱视场效应的影响。但是, 在城市地表方向亮温的近地面测量时, 热像仪与被观测目标的距离始终有限, 为了让热红外传感器视场范围之内的地物具有代表性, 往往使用大视场角测量。例如, Soux 等(2003), Lagouarde 等(2004)和 Voogt(2008)都曾使用较大的视场角观测典型城市地表。然而, 当传感器位于卫星轨道时, 卫星的成像方式与地面热辐射测量相比有着较大的区别。卫星成像的单个像元成像属于特窄视场, 并且距离城市地表目标近似于无限远处。这能导致地面观测目标发生变化, 最终产生视场效应。如余涛等(2004)使用简化三分量的二维结构模型, 对垄行植被的视场效应进行了初步分析和估算。李丽等(2006)利用“网格模型法”对垄行作物进行了视场效应的研究。

目前, 对视场效应定量化的研究仅限于在植被方面, 对于城市地表的视场效应的定量研究较少, 并且许多研究未能脱离简单的二维模拟方法。本文借助 OpenGL 三维模拟的优势, 利用辐射度原理模拟城市三维目标各组分在传感器视场内的组分比例(Soux 等, 2003; Voogt, 2008; 马伟等, 2008)。通过模拟传感器分别位于近地面和卫星轨道处的方向亮温差, 结合野外观测试验获取的组分温度和方向亮温, 对视场效应的大小和影响进行定量分析。

收稿日期: 2008-12-24; 修订日期: 2009-03-05

基金项目: 国家自然科学基金项目(编号: 40771136、40701114); 北京市优秀人才培养资助项目(编号: 20081D0503100254)。

第一作者简介: 占文凤(1986—), 男, 2007 年毕业于武汉大学遥感信息工程学院, 获学士学位。现于北京师范大学攻读博士研究生, 研究方向为资源环境遥感。E-mail: zhanwenfeng@ires.cn。

通讯作者: 陈云浩, E-mail: cyh@ires.cn。

2 模 型

2.1 方向亮温与组分温度

传感器在第 i 通道内探测到的辐射测量值与方向亮温之间满足如下关系式(Noman & Becker, 1995):

$$B_{\mathrm{b},i}(\theta,\phi)=\int_{\lambda_1}^{\lambda_2}\frac{f_i(\lambda)C_1}{\pi\lambda^5[\exp(\frac{C_2}{\lambda T_{b,i}(\theta,\phi)})-1]}\mathrm{d}\lambda \tag{1}$$

式中, $B(T_{b,i}(\theta,\phi))$ 为光谱辐亮度; λ_1 为该通道波长的下限; λ_2 为该通道波长的上限; $f_i(\lambda)$为传感器的波谱响应函数; C_1=3.7404×10^{8}W·μm^4·m^{-2}; C_2=14387μm·K; $T_{\mathrm{b},i}(\theta,\phi)$ 为该通道的亮度温度。假定一个像元由 N 种组分构成, 该像元区域内目标的方向亮温与区域内各组分的组分温度之间满足关系式(Menenti 等, 2008; 余涛等, 2006a; 黄华国等, 2007b):

$$B_\lambda(T_{\mathrm{b}}(\theta,\phi))=\sum_{k=1}^{N}f_k(\theta,\phi)\varepsilon_k B_\lambda(T_k) \tag{2}$$

式(2)中, $B_\lambda(T_{\mathrm{b}}(\theta,\phi))$ 为 Plank 函数。$T_{\mathrm{b}}(\theta,\phi)$ 为方向亮温; $f_k(\theta,\phi)$ 为在传感器视场内各个组分所占的比例, 且满足$f_1+f_2+\cdots+f_N=1$; ε_k 为各组分的发射率; T_k 为各组分的组分温度。由式(2)可知, 组分分类与传感器视场内各组分所占比例 $f_k(\theta,\phi)$是影响方向亮温的两个重要因素。

2.2 城市目标结构简化

本文将典型城市目标简化成具有三维空间结构的一系列规则的长方体(Soux 等, 2003; 马伟等, 2008)。使用辐射度的方法确定城市地表各种组分面积。如图 1, O 为传感器在空间的位置, S_1 为卫星传感器对应的一个像元大小的城市区域, 在一个像元内, 包含有各种类型的城市地表。S_2 为以 O 为球心, 1 个单位为半径的单位球半球面。S_3 为传感器的“等效焦平面”, P_1 为某一栋城市建筑物的房顶平面, P_2 为该房顶在 S_2 上的投影面。P_3 为 P_2 在等效焦平面 S_3 内的投影。房顶对应的组分权重 f_{roof} 的解析形式如下(Baum 等, 1989):

$$f_{\mathrm{roof}}=\frac{1}{2\pi}\sum_{i=0}^{3}|\boldsymbol{\Psi}\cdot\boldsymbol{\Gamma}_i| \tag{3}$$

式(3)中, $\boldsymbol{\Psi}$是平面 S_3 的法方向的单位向量; $\boldsymbol{\Gamma}_{\mathrm{i}}$的大小为向量 $\boldsymbol{R}_{\mathrm{i}}$与向量 $\boldsymbol{R}_{\mathrm{i+1}}$的夹角$\delta_i$, 用弧度表示, 方向为 $\boldsymbol{R}_{\mathrm{i}}\times\boldsymbol{R}_{\mathrm{i+1}}$所指的方向。组分权重 f_{roof}的几何意义为屋顶 P_1 的在“等效焦平面”内的投影 P_3 面积与 S_3 的面积之比(孙家广, 2005)。

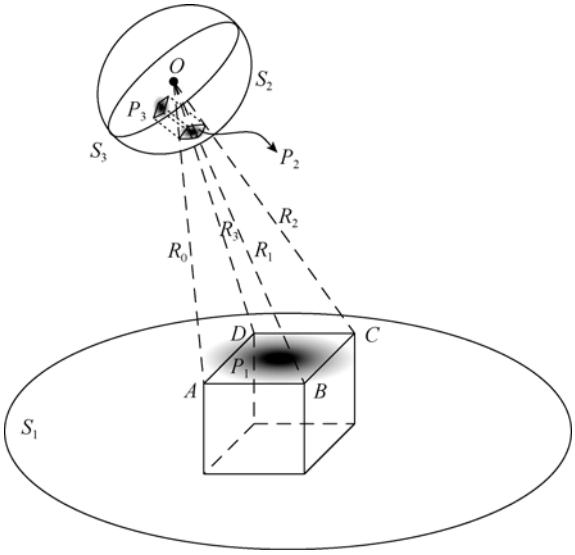

图 1 组分权重的几何意义(孙家广, 2005, 有改动)

3 组分比例模拟

已有的研究表明, 组分的物理属性、是否被阳光照射、组分所在的平面与太阳光线所构成的夹角是影响城市地物温度高低及变化的主要因素(Jackson 等, 1979; Li & Strahler, 1985; 李小文等, 1995; 余涛等, 2005)。余涛等(2006b)在对城市目标进行野外实测后, 在计算机模拟模型中将城市目标划分成亮土地、暗土地、亮楼顶、亮墙面和暗墙面 5 类。根据我们在实验中采用固定式测温仪连续观测地表温度变化的野外观测经验, 本文将典型城市目标分成光照地面、光照墙面、光照屋顶、阴影地面和阴影墙面 5 种组分类型(马伟等, 2008)。

为了分析城市目标的热辐射方向性规律, 选取了几块典型的北京城市居民小区, 在对建筑物尺寸、朝向以及东西向和南北向街道宽度调查统计后, 在 3DSMax 中制作了“城市目标实体模型”, 采用计算机模拟模型, 对各种组分的组分权重进行模拟(马伟等, 2008)。模型属性参数如表 1。

表 1 模拟模型属性参数

模型的属性参数	属性参数取值
观测时间	2008-08-22 10:40(北京时间)
东西向建筑物宽度/m	15
东西向街道宽度/m	5
南北向建筑物宽度/m	10
南北向街道宽度/m	12.5
建筑物高/m	13
视场角大小/°	20

3.1 视点位于卫星轨道

相对于地表目标，卫星传感器属于特窄视场观测，并且近似处于无限远处。图 2 是以方位角为极坐标系的角坐标、天顶角为极坐标系的距离坐标作光照墙面和阴影墙面组分权重极化图。方位角 φ 的范围为 $0°<\varphi<360°$；天顶角 θ 的范围为 $0°<\theta<60°$。S 为太阳位置。

由图 2 可知，光照墙面和阴影墙面的“组分权重——极化图”的极值基本处于太阳的主平面附近。这说明，不管太阳位置如何变化，两种组分始终受到太阳位置的强烈影响。对于光照墙面，组分权重大的地方位于“热点”位置周围；阴影墙面与此相反。另外，这两种组分在极化图中随着方位角的变化有着明显的“阶跃”特性，而随着天顶角的变化并没有明显的规律。例如，上午 10:40 时，太阳的位置如图 2(a)，当方位角 $270°<\varphi<360°$时，光照墙面的组分权重很小，当 $\varphi=270°$，$\varphi=360°$方位角时，组分权重的大小急剧变化。下午 14:30 时，太阳的位置如图 2(b)，当方位角 $90°<\varphi<180°$时，光照墙面的组分权重很小，且当方位角 $\varphi=90°$，$\varphi=180°$时，组分权重的大小急剧变化。

由于两个时刻之间太阳方位角处于 90°和 270°之间，光照地面组分权重极化图在南半平面的权重平均值要高于北半平面，阴影地面与此正好相反。太阳位置对这两种的组分权重的影响并不明显。

3.2 视点位于近地面

3.2.1 天顶角和方位角变化

与传感器的视点处于卫星轨道时相比，在近地面对方向亮温进行观测时，传感器与被测目标有限的距离造成了组分比例急剧变化。如图 3 为视点在近地面时光照墙面和阴影墙面的组分权重——极化图(模拟时，固定视场角为 17°；固定传感器距目标中心的距离为 300m)。方位角 φ 和天顶角 θ 的范围与图 2 一致。S 为太阳位置。

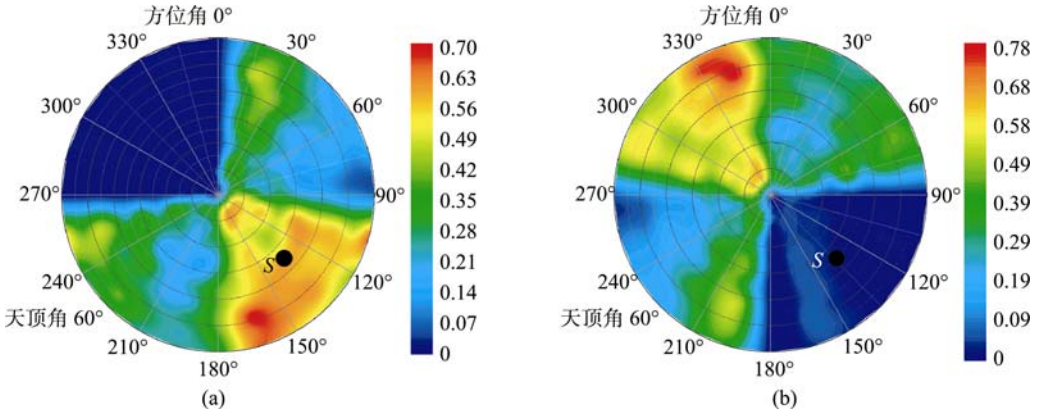

图 2 传感器位于卫星轨道时组分权重极化图

(a) 光照墙面组分比例; (b) 阴影墙面组分比例

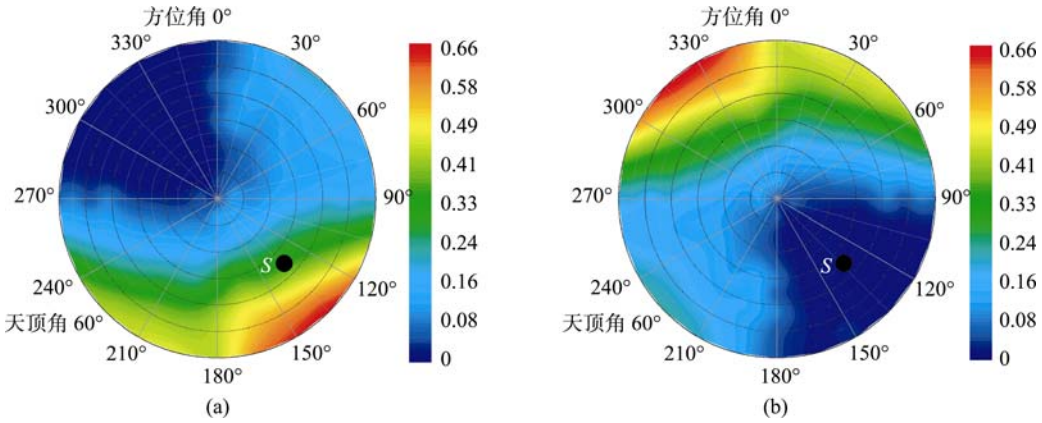

图 3 传感器位于近地面时组分权重——极化图 (视场角为 17°；观测距离为 300m)

(a) 光照墙面组分比例; (b) 阴影墙面组分比例

由图 3 可知，光照墙面和阴影墙面两种组分仍然受到太阳位置的强烈影响。图 3 中光照墙面和阴影墙面的组分比例的极值的分布区域与图 2 相似。但是，图 3 中极小值的分布区域更为广泛，而且组分比例的“阶跃”特性没有图 2 明显，随着方位角 φ 的变化，组分权重的变化更为“缓和”。更多的模拟分析表明，光照屋顶的组分比例不受太阳位置影响，其变化范围为 0.30—0.38，要小于传感器处于卫星轨道时的变化范围。当传感器处于近地面时和处于卫星轨道时各个组分的组分比例差异是很大的，在极坐标图内的变化规律也不相同。说明当传感器处于近地面时与处于卫星轨道时有着较大的差别，存在显著的视场效应。

3.2.2 观测距离变化

图 4 为当固定天顶角和方位角，传感器距目标中心的距离等间隔递增时，光照墙面和阴影墙面随着观测距离变化的组分权重变化图。图 4 中的实线值代表了当视点处于卫星轨道处时的组分权重。

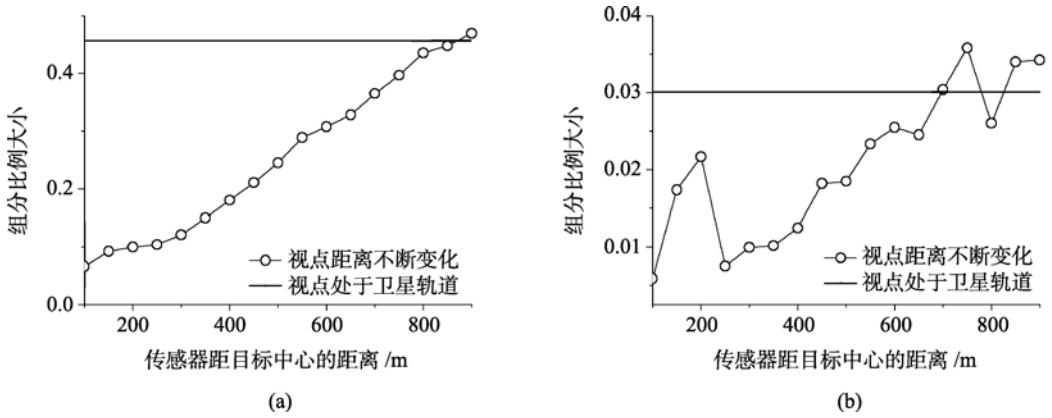

图 4 光照墙面和阴影墙面的组分比例随观测距离的变化图 (天顶角=10°; 方位角=120°)

(a) 光照墙面组分比例随观测距离的变化; (b) 阴影墙面组分比例随观测距离的变化

由图 4 可知，随着传感器与目标中心距离的增大，组分比例的大小也急剧变化。模拟时视点基本处于太阳方向，即热点方向，因此，在视点位置所观测到的光照墙面的组分比例大小较之阴影墙面高一个数量级是合理的。由于阴影墙面组分比例所占的份额极小，随着距离的增大，阴影墙面的组分比例出现了轻微的振荡。对于表 1 中的模拟模型属性参数，当观测距离为 800m 左右时，传感器观测到的组分比例与传感器位于卫星轨道处时观测到的组分比例的差别已经很小。这时，视场效应可以忽略不计，后面的观测实验中将再次得到证明。

4 试验分析

为了定量地分析视场效应的大小，本文定义“方向亮温差”，它是指当传感器处于近地面时的方向亮温与传感器处于卫星轨道处时的方向亮温之差，用其表征视场效应的大小。即亮温差的绝对值越大，则视场效应大；反之则越小。以上有关组分比例的模拟分析是视场效应分析的基础，为了衡量传感器位于近地面和位于卫星轨道处由组分比例差异导致的视场效应大小，进一步探究视场效应的变化规律，分析两种情况下的方向亮温差很有必要。

我们于 2008 年 8 月在北京师范大学房山实验基地进行了观测实验。实验中，使用自制的多角度热红外辐射近地面观测系统(图 5)。支架能够根据刻盘，按照一定的角度旋转，以保证观测的准确度。使用

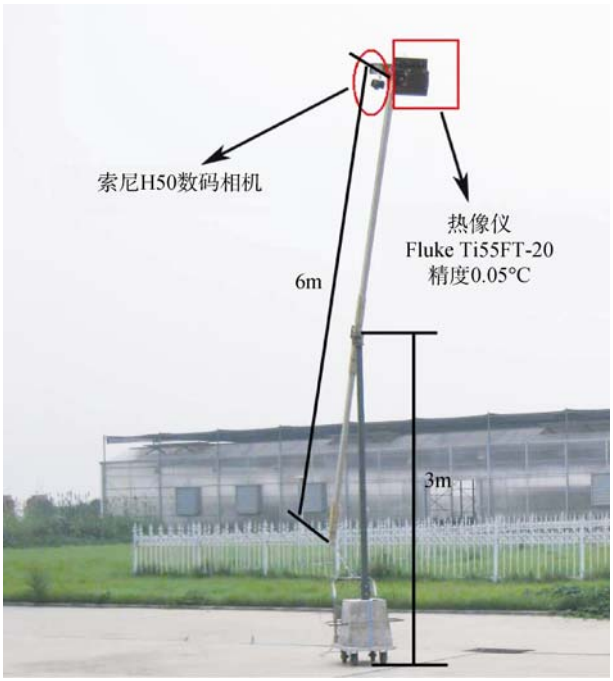

图 5 多角度热红外辐射近地面观测系统

黑体对热像仪做精确的温度定标，标定之后的温度即可作为方向亮温的实验测量值。热像仪的精度较高(0.05°C)，能够满足实验分析的要求。

观测目标为按照真实城市目标以一定比例缩小的城市目标物理模型(图 6(a), (b))。房屋物理模型的表面为水泥质地。因为铝金属的发射率很小，采用铝框来圈定研究范围，模型的属性参数如表 1 所示(缩小比例为 1:50)。如图 6(a)为数码相机获得的可见光影像；图 6(b)为热像仪获得的热红外影像，颜色越亮表征温度越高。

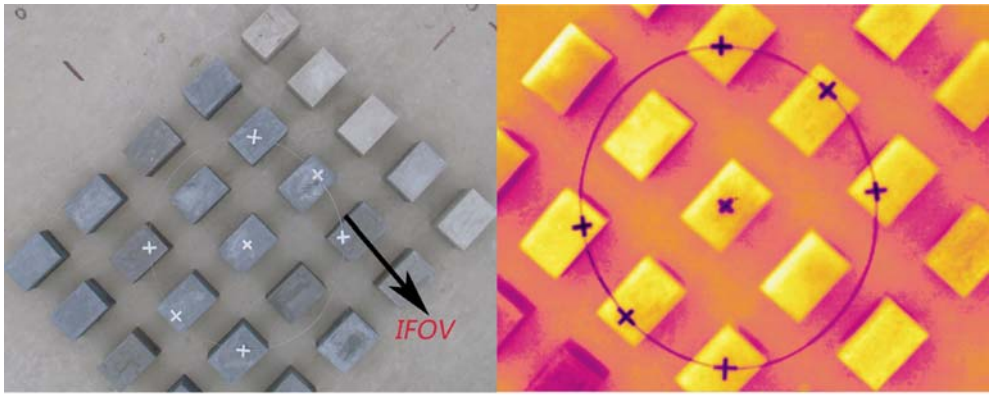

图 6　真实城市目标 1：50 比例缩小的城市目标物理模型所得到的可见光以及热红外图像
(铝框所示的范围为 IFOV 的大小)
(a) 相机所获得的可见光影像; (b) 热像仪所获得的亮温数据

为了说明视场效应随天顶角、方位角和观测距离的变化情况，采取了实验测量+计算机模拟的方式。计算机模拟模型需要将组分温度作为模型输入值。为此，选取上午 10: 40 与下午 14: 30 两个时刻，采用手持式红外测温仪(型号: Testo-845)测量了各个组分的组分温度。经黑体标定，各组分的组分温度值如表 2。

表 2　各组分的组分温度

观测时间	光照地面/°C	光照墙面/°C	光照屋顶/°C	阴影地面/°C	阴影墙面/°C
10: 40	36.8	48.9	51.2	26.5	33.3
14: 30	41.0	48.2	50.3	30.7	37.0

4.1　不同方位角和天顶角视场效应分析

图 7 为根据各组分温度和计算机模型模拟的两个时刻的亮温差——极化图。从图中可知，上午 10: 40 时亮温差的变化范围为−4.42°C—3.18°C；绝大多数的天顶角和方位角处的亮温差处于±1°C 之间。下午 14：30 时亮温差的变化范围为−3.18°C—3.46°C，说明上午和下午两个时刻的视场效应大小相当。S 为太阳位置，P 为太阳主平面的垂面。图 7(a)和图 7(b)中，M_1 是方向亮温差的极大值区域。M_2，M_3 是方向亮温差的极小值区域。亮温差的极大值和极小值位于平面 P 附近，当传感器的天顶角 θ<60°时，在垂直

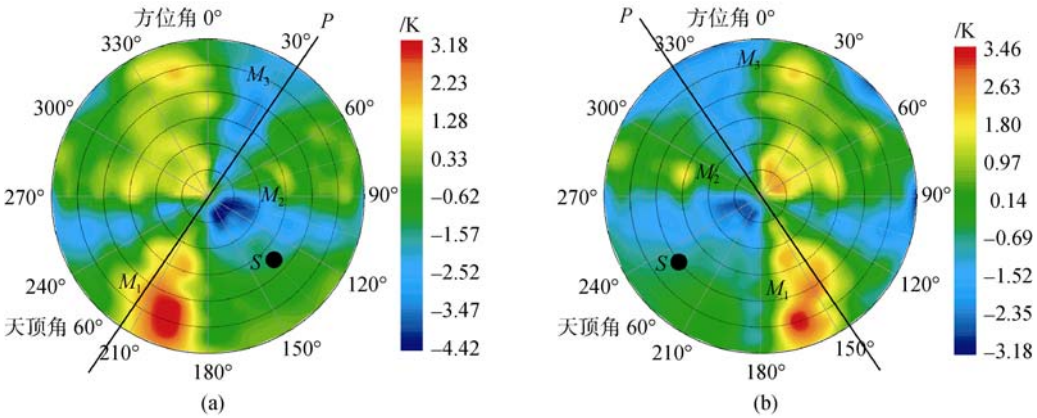

图 7　方向亮温差——极化图 (观测距离为 300m)
(a)10:40; (b)14:30

太阳主平面附近，视场效应较大。

当传感器位于近地面时，必须使用较大的视场角；而当传感器位于卫星轨道上时，单个像元对应的视场角极小。上午时分，当 $\varphi\in[0°, 90°]$和 $\varphi\in[180°, 270°]$时，这种视场角的巨大差异造成图 2 中的组分权重分布在如上的两个区间内显著的阶跃特性，相对图 2 来说，图 3 中的组分权重在两区间内变化较为缓和，说明在这两个区间内相同组分的组分权重差异明显，视场效应较大。同时，由于上午太阳方位角 $\varphi\in[90°, 180°]$，这时太阳的主平面在集合 $\varphi\in\{[90°, 180°],[270°, 360°]\}$内，太阳主平面的垂面则在集合 $\varphi\in\{[0°, 90°],[180°, 270°]\}$内(图 7(a))。下午亦有类似关系(图 7(b))。这意味着在太阳主平面的垂面附近，视场效应较大。

4.2 不同观测距离的视场效应分析

为了探讨随着观测距离改变，由视场效应造成的方向亮温差的变化情况，使用多角度热红外观测系统实测方向亮温值与计算机模拟值(因为实验测量无法得到在卫星轨道处的方向亮温，只能采取计算机模拟的方式)结合起来，得到方向亮温差随观测距离改变的变化图。如图 8(a), (b)所示。上午 10∶40，选用的固定方位角和天顶角为图 7(a)的极大值区域 M_1(方位角=200°；天顶角=45°)和极小值区域 M_2(方位角=120°；天顶角=10°)。下午 14∶30，选用的固定方位角和天顶角为图 7(b)的极大值区域 M_1(方位角=150°；天顶角=40°)和极小值区域 M_2(方位角=240°；天顶角=10°)。

由图 8(a),(b)可知，观测距离越近，视场效应越大；反之，观测距离越远，则视场效应越小。即视场效应的尺度效应显著。当观测距离 L>800m 时，由观测距离造成的视场效应小于 0.2°C，可忽略不计；当观测距离 200m<L<800m 时，观测距离与视场效应的大小(亮温差的绝对值)大致呈现线性的反比关系；而当观测距离 L<200m 时，规律较为复杂，既有急剧增大的(如图 8(a)中方位角=120°；天顶角=10°和图 8(b)中方位角=240°；天顶角=10°)，又有略微减少的(如图 8(a)中方位角=200°；天顶角=45°和图 8(b)中方位角=150°；天顶角=40°)。这是因为随着观测距离减少到一定程度，在传感器的视场范围内地物的种类不断减少，到最后甚至只剩下某一种地物。很显然，这时方向亮温的大小完全取决于该种组分的组分温度，而观测到的组分类型又具有随机性，因此当观测距离 L<200m 时，虽然视场效应较大，但分布规律不明显。

4.3 时间序列视场效应分析

为了分析视场效应随时间的变化，选用观测时间为 2008-08-23, 10∶40—12∶00 的数据。期间，太阳方位角从 136°变化到 171°。方位角为东、西、南、北、东北、东南、西南、西北 8 个方向。根据天顶角的差别，观测试验包括 3 轮，每一轮的观测包括如上 8 个方向的观测。每次观测大概持续 3min，一轮观测试验约为 25min。

图 9 为方向亮温差随时间的变化图。所有的散点分布在 0℃左右，亮温差的变化范围为–3°C—4℃。另外，每一轮的亮温差的变化范围大致相当。第 3 轮的视场效应比第 1、2 轮略小。这是因为第 3 轮的观测时间接近中午，与第 1 轮和第 2 轮相比，组分间温差减小许多。由图 7—图 9 可知，不同空间位置和时间序列的视场效应的分析结果表明亮温差的变化范围为±4℃。

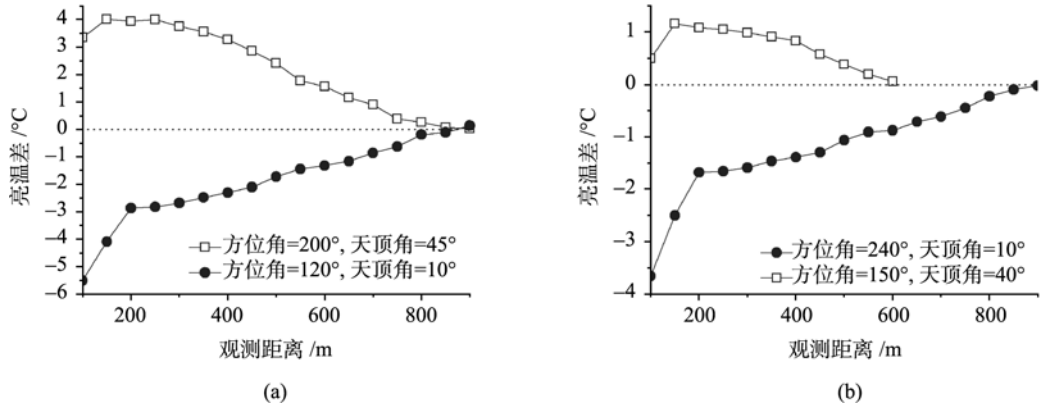

图 8 方向亮温差随观测距离改变的变化

(a) 10:40; (b) 14:30

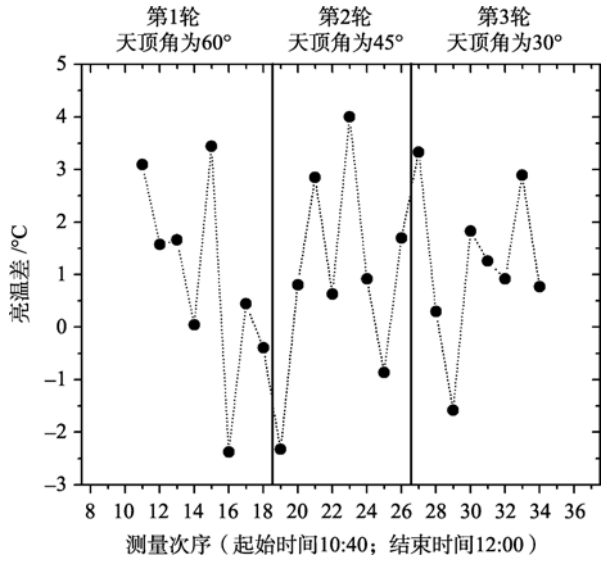

图 9　方向亮温差随观测角度和时间的变化图
(观测距离为 300m)

5　结　论

本文针对典型城市地表，对比分析了传感器分别位于卫星轨道和近地面进行观测时，传感器视场内各组分的组分比例随空间位置变化的变化规律。模拟结果表明，城市地表的近地面方向亮温测量存在着显著的视场效应。最后分析了视场效应随传感器的天顶角、方位角和观测距离变化的变化规律。结果表明，垂直太阳主平面附近的视场效应最大；随着观测距离的增加，视场效应急剧减少。而且，对空间不同位置和时间序列的视场效应分析表明方向亮温的视场效应明显。

与植被热辐射方向性研究不一样的是，针对城市地表热辐射方向性规律的研究仍然不成熟。典型城市地表上既有高大乔木，又有低矮的灌丛和草地，还有裸地、不同材质的屋顶和墙面等等。城市建筑物高大，与低矮的行播农作物相比，仪器架设、野外观测实验等较为困难。而物理模型则不失为一个研究典型城市建筑热辐射规律的替代工具。

影响视场效应的众多因素会影响到城市地表方向亮温观测的视场效应。地表-大气是一个耦合系统，它们之间的能量交换影响地表各种组分的温度分布规律，进一步带来了方向亮温视场效应变化的复杂性。本文仅对视场效应的尺度效应开展了初步的定性分析，仍存在很多不足，针对尺度效应的定量分析，后续的野外试验和计算机理论模拟研究也正在积极展开。

REFERENCES

Baum D R, Rushmeier H E and Winget J M. 1989. Improving radiosity solutions through the use of analytically determined form-factors. *Computer Graphics*, **23**(3): 325—333

Fan W J and Xu X R. 2003. The Affecting factors of thermal radiant drectionality of the row winter wheat. *Geography and Geo-Information Science*, **19**(4): 84—88

Huang H G, Liu Q H, Liu Q, Du Y M and Li X W. 2007. Simulation of time effect on thermal emission directionality measurement. *Journal of System Simulation*, **19**(15): 3586—3590

Huang H G, Liu Q H, Liu Q, Xiao Q and Chen L F. 2007. Using multi-directional thermal images to obtain canopy component temperature and directional brightness temperature. *Journal of Beijing Normal University*(*Natural Science*), **643**(3): 292—297

Jackson R D, Raginato R J, Pinter P J, Jr and Sherwood B. I. 1979, Plant canopy information extracton from composite scene reflectance of row crops. *Applied Optics*, **18**(22): 3775—3782

Lagouarde J P, Kerr Y H and Brunet Y. 1995. An experimental study of angular effects on surface temperature for various plant canopies and bare soils. *Agricultural and Forest Meteorology*. **77**: 167—190

Lagouarde J P, Moreau P, Irvine M, Bonnefond J M, Voogt J A and Folliec F. 2004. Airborne experimental measurements of the angular variations in surface temperature over urban areas: case study of Marseille(France). *Remotes Sensing of Environment*, **93**: 443—462

Li L, Qiao Y L, Gu X F and Yu T. 2006. Field of view effect on the remote sensing field radiometric measurements. *Journal of Remote Sensing*, **10**(5): 676—682

Li X W and Strahler A. 1985. Geometric-optical modeling of a conifer forest canopy. *IEEE Trans Geosci Remote Sensing*, **23**(5): 705—721

Li X W and Wang J D. 1995. Optical Remote Sensing Model and Parameterization for Vegetation. Beijing: Science Press

Ma W, Chen Y H, Zhan W F and Zhou J. 2008. A computer model for simulating the thermal infrared radiation of 3-D urban targets. *Journal of Infrared and Millimeter Waves*, In Press

Menenti M, Li J and Li Z L. 2008. Multi-angular thermal infrared observations of terrestrial vegetation. Advances in Land Remote Sensing System, Modeling, Inversion and Application. Springer

Noman J M and Becker F. 1995. Terminology in thermal infrared remote sensing of natural surfaces. *Agricultural and Forest Meterology*, **77**: 153—166

Soux A, Voogt J A and Oke T R. 2003. A model to calculate what a remote sensor ‘sees’ of an urban surface. *Boundary-Layer Meteorology*, **111**: 109—132

Sun J G et al. 2005. Computer Graphics. Beijing: Tsinghua University Press

Voogt J A and Oke T R. 2003. Thermal remote sensing of urban climates. *Remote Sensing of Environment*. **86**: 370—384

Voogt J A. 2008. Assessment of an urban sensor view model for thermal anisotropy. *Remote Sensing of Environment*, **112**: 482—495

Wang J D, Li X W, Sun X M and Liu Q.2000. Component temperatures inversion for remote sensing pixel based on directional thermal radiation model. *Science in China*(*Ser. E*), **30**(supp.): 54—60

Yu T, Gu X F, Tian G L, Legrand M, Hanocq J F and Bosseno R. 2004. Analyzing the errors caused by FOV effect on the ground observations of drectional brightness temperature over a row Structured canopy. *Journal of Remote Sensing*, **8**(5): 443—450

Yu T, Gu X F, Tian G L, Legrand M, Hanocq J F, Bosseno R and Cai H Y. 2005. Study on the classification of component brightness temperature over a maize canopy. *Jounal of Remote Sensing*, **9**(1): 16—23

Yu T, Gu X F, Tian G L, Legrand M, Hanocq J F, Bosseno R, Cai H Y, Cheng T H and Yu S S. 2006. Modeling directional brightness temperature over a maize canopy in row structure. *Journal of Remote Sensing*, **10**(1): 15—20

Yu T, Tian Q Y, Gu X F, Wang J, Liu Q and Yan G J. 2006. Modelling directional brightness temperature over a simple typical structure of urban areas. *Journal of Remote Sensing*, **10**(5): 661—669

Zhang R H, Sun X M, Li Z L, Stoll M P, Su H B and Tang X Z. 2000. Revealing of major factors in the directional thermal radiation of ground objects. *Science in China*(*Ser. E*), **30**(supp.): 39—44

Zhou J, Chen Y H, Li J, Ma W and Zhan W F. 2009. Progress in thermal anisotropy of urban areas: a review. *Advances in Earth Science*, **24**(5):497—505

附中文参考文献

范文捷, 徐希孺. 2003. 行播冬小麦辐射方向性的影响因子. 地理与地理信息科学, **19**(4): 84—88

黄华国, 柳钦火, 刘强, 杜永明, 李小文. 2007. 热辐射方向性测量中的时间效应模拟. 系统仿真学报, **19**(15): 3586—3590

黄华国, 柳钦火, 刘强, 肖青, 陈良富. 2007. 利用多角度热图像提取冠层组分温度和方向亮温. 北京师范大学学报(自然科学版), **643**(3): 292—297

李丽, 乔延丽, 顾行发, 余涛. 2006. 遥感地面辐射观测中的视场效应问题研究. 遥感学报, **10**(5): 676—682

李小文, 王锦地. 1995. 植被光学遥感模型与植被结构参数化. 北京: 科学出版社

马伟, 陈云浩, 占文凤, 周纪. 2008. 城市三维目标热辐射计算机模型研究. 红外与毫米波学报, 待发表.

孙家广等. 2005. 计算机图形学, 北京: 清华大学出版社

王锦地, 李小文, 孙晓敏, 刘强. 2000. 用热辐射方向性模型反演非同温像元组分温度. 中国科学(E 辑), **30**(增刊): 54—60

余涛, 顾行发, 田国良, Legrand M, Hanocq J F, Bosseno R, 蔡红艳, 程天海, 余珊珊. 2006. 垄行结构玉米冠层方向亮温模型研究. 遥感学报, **10**(1): 15—20

余涛, 顾行发, 田国良, Legrand M, Hanocq J F, Bosseno R, 蔡红艳. 2005. 玉米组分亮度温度分类变化研究. 遥感学报, **9**(1): 16—23

余涛, 顾行发, 田国良, Legrand M, Hanocq J F, Bosseno R. 2004. 垄行作物玉米方向亮温野外观测测量中视场角影响的简单分析. 遥感学报, **8**(5): 443—450

余涛, 田启燕, 顾行发, 王进, 刘强, 闫广建. 2006. 城市简单目标方向亮温研究. 遥感学报, **10**(5): 661—669

张仁华, 孙晓敏, 李召良, Stoll M P, 苏洪波, 唐新斋. 2000. 地物热辐射方向性影响主因子揭示. 中国科学(E 辑), **30**(增刊): 39—44

周纪, 陈云浩, 李京, 马伟, 占文凤. 2009. 城市区域热辐射方向性研究进展. 地球科学进展, **24**(5): 497—505